This is a repository copy of *Erosion-corrosion interactions of X65 carbon steel in aqueous CO₂ environments*.

Erosion-corrosion interactions of X65 carbon steel in aqueous CO₂ environments

Joshua Owen[a], Callum Ramsey[b], Richard Barker[a], Anne Neville[a]

[a] Institute of Functional Surfaces, School of Mechanical Engineering, University of Leeds, Leeds, LS2 9JT, United Kingdom
[b] Shell U.K. Limited, 1 Altens Farm Road, Nigg, Aberdeen, AB12 3FY, United Kingdom

Abstract

When sand is present in carbon dioxide (CO_2) corrosion environments in carbon steel oil and gas pipelines, wear rates can be particularly severe. The wear mechanism when surfaces are exposed to impact by a solid-laden corrosive fluid is known as erosion-corrosion and consists of erosion and corrosion components with total erosion-corrosion degradation enhanced by interactions between erosion and corrosion. The causes of corrosion-enhanced erosion and erosion-enhanced corrosion of carbon steel, in this regime, are not fully understood and are the subject of study in this work in a 60°C, pH 4.7, 2% NaCl solution, containing 1000 mg/L of sand particles with an average diameter of 250 μm, flowing through a submerged impinging jet (SIJ) nozzle at 20 m/s. Particle impact angles and velocities were predicted on the SIJ sample surface using computational fluid dynamics (CFD) to improve the understanding of how particle impingement contributes to erosion-enhanced corrosion and corrosion-enhanced erosion. Corrosion-enhanced erosion accounted for up to 20% of total erosion-corrosion degradation, with focused ion beam scanning electron microscopy (FIB-SEM) analysis showing that removal of work hardened layers and subsurface cracking were causes of enhanced degradation. Erosion-enhanced corrosion was not significant in the conditions tested.

1. Introduction

Erosion-corrosion is a complex mechanism of material degradation that affects many industries, including oil and gas. The process consists of electrochemical and mechanical degradation, as well as their potential combined synergistic effects [1]. The presence of carbon dioxide (CO_2) in oil and gas produced fluids results in a corrosive environment, and the entrainment of sand particles in the corrosive flow results in a highly aggressive wear

environment for carbon steel pipelines. Due to the high rates of degradation carbon steel pipelines can experience in erosion-corrosion conditions, as well as production and maintenance requirements in the oil and gas industry, understanding erosion-corrosion and identifying effective methods to protect pipelines is important. Erosion-corrosion is complicated by the interaction between erosion and corrosion, whereby erosion-corrosion degradation rates can be dramatically higher than the sum of the individual erosion and corrosion rates, as defined by Equation (1), with erosion enhancing corrosion and corrosion enhancing erosion processes [2].

$$EC_{TML} = C + E + \Delta C_E + \Delta E_C \qquad (1)$$

where EC_{TML} is the total erosion-corrosion material loss, C is the pure corrosion rate, E is the pure erosion rate, ΔC_E is the erosion-enhanced corrosion and ΔE_C is the corrosion-enhanced erosion.

CO_2 corrosion is an electrochemical process, consisting of anodic and cathodic reactions. When CO_2 dissolves in water, it hydrates to produce carbonic acid (H_2CO_3). H_2CO_3 partially dissociates in two steps, resulting in the formation of bicarbonate, carbonate and hydrogen (H^+) ions [3]. The main cathodic reaction that occurs at the steel surface in CO_2 environments at pH ~ 4 is direct reduction of H^+ ions, Equation (2). Direction reduction of H_2CO_3, Equation (3), has also been reported, however, some debate exists about the mechanisms of this reaction, as it has been suggested that H_2CO_3 dissociates at the steel-electrolyte interface, producing H^+ ions that are subsequently reduced at the steel surface [3, 4]:

$$2H^+ + 2e^- \rightarrow H_2 \qquad (2)$$

$$2H_2CO_3 + 2e^- \rightarrow H_2 + 2HCO_3^- \qquad (3)$$
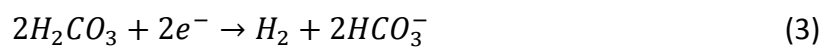
The anodic reaction, the electrochemical dissolution of iron, can be summarised using Equation (4).

$$Fe_{(s)} \rightarrow Fe^{2+}_{(aq)} + 2e^- \qquad (4)$$

However, it is important to note that the dissolution of iron consists of a series of reactions involving the generation and consumption of various intermediate products prior to an iron ion being produced [5, 6].

Interactions between erosion and corrosion have been the subject of several studies, with the majority of work focused on passive alloys [1, 7-9]. Carbon steel erosion-corrosion research has often been limited to quantifying interactions through parametric testing [9-11]. Several theories have been suggested to explain the causes of interactions. Erosion has been thought to enhance corrosion through surface roughening from particle impingements, and through mechanical removal of protective passive films or corrosion inhibitor films used to protect carbon steel surfaces [2, 12]. The surface roughness of ductile metals is known to increase after particle impingement [13]. A higher surface roughness can result in increased mass transfer of corrosive species to the material surface, enhancing corrosion rates [14]. Increasing the metal surface roughness also exposes more material surface area, increasing dissolution rates [15]. Surface roughening could also change local flow conditions near to the surface of the target material which could influence particle trajectories in addition to corrosion rates [16].

Corrosion of work hardened layers exposing the underlying softer material is thought to be one of the main causes of corrosion-enhanced erosion [2, 17]. Plastic deformation, caused by particle impacts on a metal surface, results in strain hardening of the material due to the movements of dislocations in the crystal structure of the metal [18]. Several materials have been shown to work harden in submerged impinging jet (SIJ) erosion tests [7, 19]. Rajahram et al. [20] used a focused ion beam (FIB) to analyse work hardened layers of UNS S31603, showing refined layers of nano-grains, less than 1 μm thick, nearest to the surface with sublayers of micro-grains formed after repeated particle impacts. Less research has been completed investigating work hardening of carbon steel and its influence on corrosion-enhanced erosion. X65, a common pipeline grade carbon steel with a ferrite-pearlite microstructure, and other ferrite-pearlite carbon steels have been shown to work harden as a result of applying strain [21-23]. Hutchings and Winter [24] completed single impact erosion tests on carbon steel using steel balls at high velocity and showed that ferrite grains were deformed from approximately 25 μm to 1 μm in size in the region closest to the surface after impact, increasing the hardness. Although not always the case, increased hardness typically results in greater erosion resistance; however, other properties, such as microstructure, can influence erosion performance of materials [23, 25]. Guo et al. [17] showed how work-hardened layers of carbon steel could be removed through corrosion; however, the removal

of work hardened layers on carbon steel has not been investigated in erosion-corrosion conditions.

Jiang et al. [26, 27] proposed that erosion rates were enhanced in erosion-corrosion conditions by micro-crack initiation and propagation, formed from a low cycle fatigue process, where multiple impacts in a region on a surface eventually produce fracture and the presence of corrosive species accelerate the growth of the crack. When cracks grow, it is expected that lips and platelets formed from particle impacts are weakened, making removal of these regions easier in subsequent particle impacts [27].

Corrosion-enhanced erosion and erosion-enhanced corrosion rates of carbon steel have regularly been quantified, but the mechanisms that contribute to enhanced degradation have rarely been investigated in conditions relevant to oil and gas pipe flow. The significance of hydrodynamic conditions and particle impingement on erosion-corrosion interactions are also largely unknown. Impact angles on sample surfaces in SIJs are often not reported but can vary significantly over the surface [28, 29]. Impact angle is particularly influential in erosion degradation mechanisms and has been reported to influence surface roughening [13]. One method of determining the impact angles and impact velocities of sand-liquid flows is by using computational fluid dynamics (CFD). CFD has been used to predict the trajectories of particles across a range of different flow geometries [29-31]. However, the use of particle impact data has often not been applied to develop the understanding of erosion-enhanced corrosion and corrosion-enhanced erosion.

This paper presents an experimental analysis of erosion-corrosion of carbon steel combined with the use of CFD to predict particle trajectories in the SIJ to develop an understanding of the mechanisms of erosion-enhanced corrosion and corrosion-enhanced erosion of X65 carbon steel and their contribution to total erosion-corrosion degradation. Several surface analysis techniques were used to determine how the properties of carbon steel surfaces were affected by erosion-corrosion conditions and how these effects contributed to enhanced rates of degradation.

2. Experimental Methodology

2.1. Erosion-Corrosion SIJ Testing

SIJs are commonly used for erosion-corrosion testing as they provide a method of quantifying each of the contributing factors to total erosion-corrosion degradation, shown in Equation (1), at high flow velocities for a range of sand particle impact angles. The SIJ used for erosion-corrosion testing in Figure 1 consisted of a reservoir with a 50 L capacity, which was filled with a brine solution containing sand particles and recirculated through a dual nozzle arrangement before impinging on to two specimens set at a distance of 5 mm below the exit of the nozzles at a velocity of 20 m/s. The flow velocity was measured at the exit of the 4 mm diameter nozzles and calibrated prior to starting the test. The temperature of the solution was maintained at 60°C throughout the test. Three types of test were completed – flow-induced corrosion (no sand), erosion (no corrosion) and erosion-corrosion to measure how each of the wear mechanisms contributed to erosion-corrosion of carbon steel. In flow-induced corrosion tests, with no sand present in the flow, the 2 wt.% NaCl, 50 L solution was saturated with CO_2 at a partial pressure of 0.54 bar. CO_2 was bubbled into the solution for a minimum period of 12 hours to reduce the dissolved oxygen concentration to less than 50 ppb (confirmed previously through the application of a colorimetric technique). Solution pH in the reservoir was maintained at pH 4.7 throughout flow-induced corrosion and erosion-corrosion tests. These conditions were chosen to replicate field conditions.
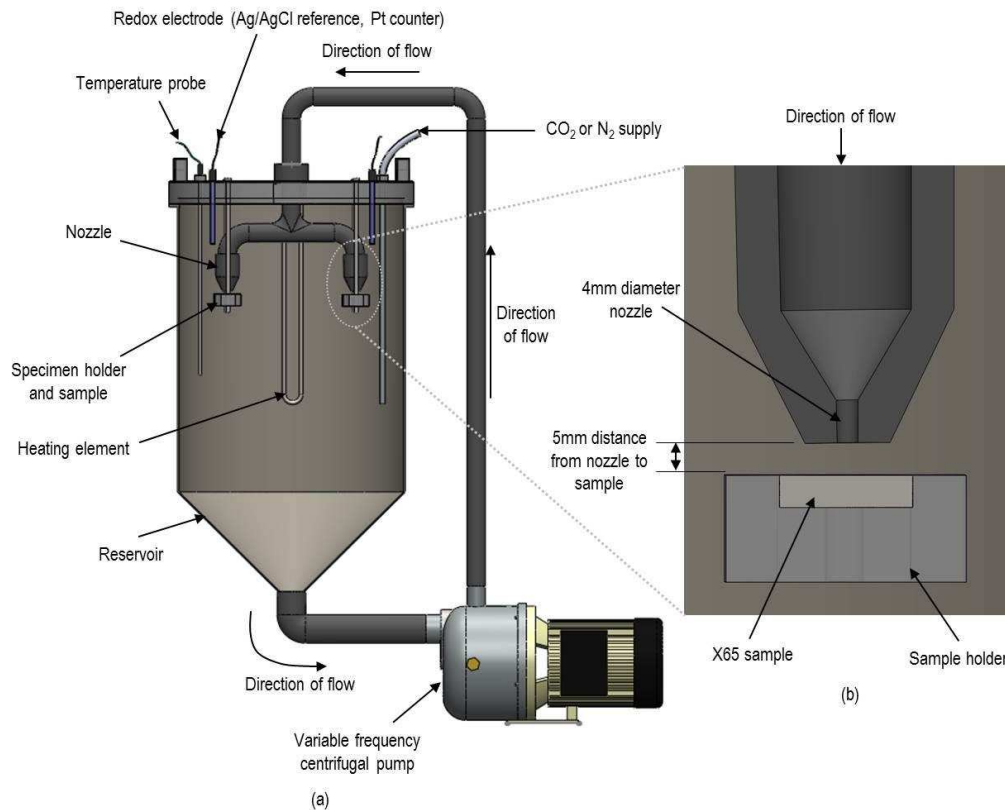
Figure 1: SIJ used for flow-induced corrosion, erosion and erosion-corrosion tests showing (a) the full SIJ apparatus and (b) a cross section of the nozzle and X65 sample

For pure erosion tests, nitrogen (N_2) was bubbled into a 2 wt.% NaCl solution, containing 1000 mg/L of HST60 sand particles with an average particle diameter of 250 µm and size distribution as shown in Figure 2. Average percentage composition is shown for size measurements from three different batches of sand particles, with the error bars representing standard deviation. Figure 2 also shows an SEM image of the sand particles, showing that particles had various irregular shapes and were not perfectly spherical. In erosion-corrosion tests, the same quantity of sand was added to a CO_2-saturated, 2 wt.% NaCl solution. Two X65 carbon steel samples, each with a surface area of 4.9 cm^2 and composition as shown in Table 1, were used in the experiments. The microstructure of an X65 sample used in SIJ testing is shown in Figure 3, observed using an optical microscope after polishing the sample using 3 µm diamond suspension paste and etching for 10 seconds in a 2% Nital solution. Ferrite grains had sizes approximately in the range of 10 µm - 25 µm.

Samples were wet-ground prior to testing to a surface finish (S_a) of 0.15 µm ± 0.02 µm, measured using a Bruker NPFLEX white light interferometer with a 0.8 mm Gaussian cut-off filter. Samples were degreased with acetone, rinsed with distilled water and dried to measure

the mass of the sample prior to the start of the test using a mass balance with a precision of ±0.01 mg. Mass loss measurements were completed in each of the three conditions (flow-induced corrosion, pure erosion, erosion-corrosion). The effect of each wear mechanism was investigated over time, with 30, 60, 120 and 240-minute length tests completed. 1, 5 and 10-minute tests were also conducted to measure the rate of work hardening of the samples in erosion conditions and in CO_2 corrosion conditions to measure the rate at which work hardened layers were removed. The average Vickers hardness of the samples, measured at multiple points on the surface after polishing, was 202 H_V ± 10 H_V.

Table 1: X65 carbon steel composition (wt. %)

C	Mn	Ni	Nb	Mo	Si	V	P	S	Fe
0.15	1.422	0.09	0.054	0.17	0.22	0.06	0.025	0.002	97.81
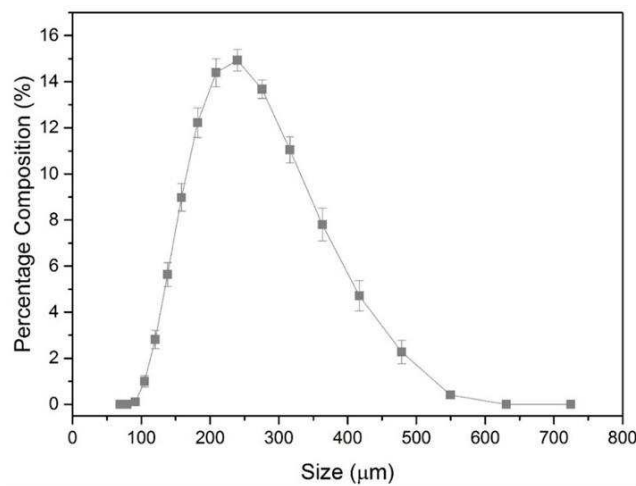
(a)
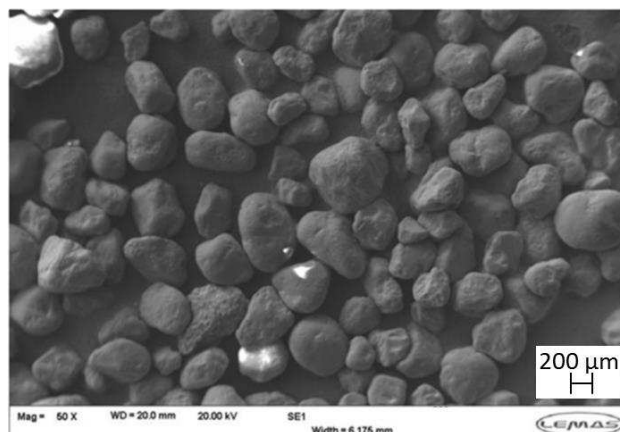
(b)

Figure 2: HST60 sand particles used in erosion and erosion-corrosion SIJ tests showing (a) size distribution of the particles and (b) SEM image of sand particles [32]
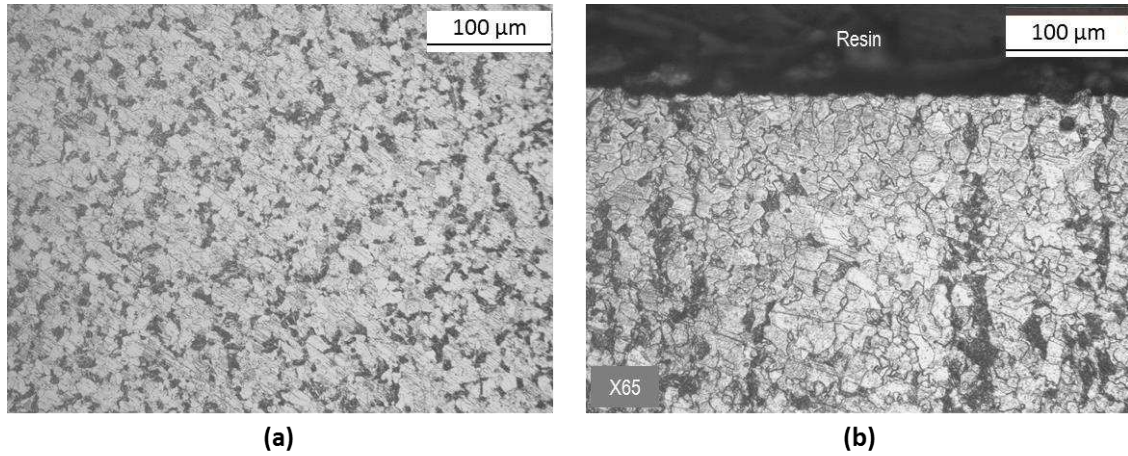
Figure 3: X65 carbon steel microstructure (a) across the surface of the sample and (b) the cross section of the sample after being etched in a 2% Nital solution for 10 seconds showing ferrite grains (lighter coloured) and pearlite regions (darker)

2.2. Electrochemical Measurements

To determine erosion-enhanced corrosion rates, electrochemistry measurements were performed in flow-induced corrosion and erosion-corrosion conditions to measure the difference in corrosion rate when sand was present in the flow. A wire was soldered to the reverse side of the X65 sample which was then embedded in non-conductive epoxy resin. A standard three-electrode cell was used, consisting of the X65 sample as the working electrode and a silver/silver-chloride (Ag/AgCl) redox reference electrode that incorporated a platinum (Pt) counter electrode. The position of the electrodes in the SIJ is shown in Figure 1. Electrochemical impedance spectroscopy (EIS) measurements were completed in a frequency range of 20,000 Hz to 0.1 Hz to measure the solution resistance (R_s) and the charge-transfer resistance (R_{ct}) and hence to determine the corrosion rate of the sample.

The corrosion current density, i_{corr}, was determined using the following equation:

$$i_{corr} = \frac{B}{R_{ct}} = \frac{1}{R_{ct}} \frac{\beta_a \beta_c}{2.303(\beta_a + \beta_c)} \tag{5}$$

where B is the Stern-Geary coefficient, β_a is the anodic Tafel constant and β_c is the cathodic Tafel constant. Tafel constants were determined by potentiodynamic sweeps after 210 minutes, to ensure the test finished within 240 minutes. The cathodic polarisation sweep was completed from +15 mV to -250 mV vs open circuit potential (OCP) at a scan rate of 0.5 mV/s prior to the anodic sweep from -15 mV to +250 mV at the same scan rate with a four-minute

8

period in between the two measurements where the OCP was allowed to stabilise. After calculating the Stern-Geary coefficient and i_{corr}, the corrosion rate was calculated:

$$V_c = \frac{K i_{corr} M_{Fe}}{n\rho} \tag{6}$$

where K is a conversion factor equal to 3.27 used to obtain the corrosion rate, V_c, in mm/year, M_{Fe} is the molar mass of iron (55.8 g/mol), n is the number of electrons in the anodic reaction (2 electrons), ρ is the density of steel (7.87 g/cm^3). A Solartron SI 1280 potentiostat was used and controlled using CorrWare software to perform potentiodynamic measurements and ZPlot to perform EIS measurements. Mass loss measurements were also completed in flow-induced corrosion conditions, which were converted into corrosion rates in mm/yr using the following equation:

$$V_c = \frac{87600\Delta m}{\rho A t} \tag{7}$$

where Δm is the mass loss of the sample in g, A is the surface area of the sample in cm^2 and t is the test duration in hours.

2.3. Surface Analysis of Samples Used in Erosion-Corrosion Tests

Several surface analysis techniques were used to analyse X65 sample surfaces after SIJ testing. 3D profiles of the surfaces were measured using a Bruker NPFLEX white light interferometer. Using the 3D profiles, the aerial surface texture (S_a) of the samples was determined. Micro-indentation of the samples was completed using a Mitotoyo HM-122 micro-indenter to determine the Vickers hardness, with an applied indentation load of 4.9 N. SEM analysis of the surfaces of samples after SIJ testing was completed using a Hitachi TM3030 Benchtop SEM to investigate the effects of particle impacts on the surface of the sample. Subsurface analysis was completed using a FEI Helios G4 DualBeam FIB-SEM. Regions on the surfaces of X65 samples used in erosion and erosion-corrosion tests were milled using a 30 kV ion beam to analyse the microstructure to a depth of approximately 15 µm below the sample surface and approximately 10 µm wide. The resulting surface after milling was then polished and etched using the ion beam. SEM analysis of the resulting surfaces after milling and polishing was completed at a magnification of 30,000x.

3. Particle Trajectory Predictions

The full range of sand particle impact angles and velocities were unknown in the SIJ for the conditions used experimentally, limiting the conclusions that could be drawn from the effect of particle impacts on erosion-corrosion results. Gnanavelu et al. [29] predicted sand particle impact angles and impact velocities on the surface of an SIJ sample using a nozzle diameter of 7 mm at a flow velocity of 5 m/s, but it was expected that the different nozzle diameter and flow velocity used experimentally in this work would change impingement characteristics on the sample surface. The combination of CFD, to predict particle trajectories in the SIJ, with experimental evaluation of carbon steel enabled a more detailed understanding of the effects of particle impacts on erosion-corrosion in the SIJ. Predicting the path of particles in the SIJ for a given velocity gave a significant amount of impact data on the sample, including impingement angles, velocities and their location on the sample surface. Analysis of the surface of samples after completing erosion-corrosion tests and correlating the surface profile and texture with the particle impact data allowed a greater understanding of the influence of sand particles on pure erosion and erosion-corrosion of carbon steel.

COMSOL Multiphysics 5.2a was used to develop a model of the SIJ to predict the trajectories of sand particles as they exit the nozzle and impinge onto a sample. The nozzle was modelled as a 2D axisymmetric system to reduce computational time and complexity, without any significant reduction in accuracy. The axisymmetric model of the SIJ nozzle is shown in Figure 4. Sand particles were modelled to enter the top of the nozzle and to flow through the nozzle onto the sample. The k-ω turbulence model was used to predict the fluid flow, with the model validated by comparing the CFD predicted shear stress with an analytical solution [33], showing approximately 13% difference in conditions where the analytical solution could be reliably applied. A mesh consisting of 81,911 first order triangular bulk domain and rectangular boundary elements was used for predictions. Full details of the model description and validation are included as Supplementary Material.
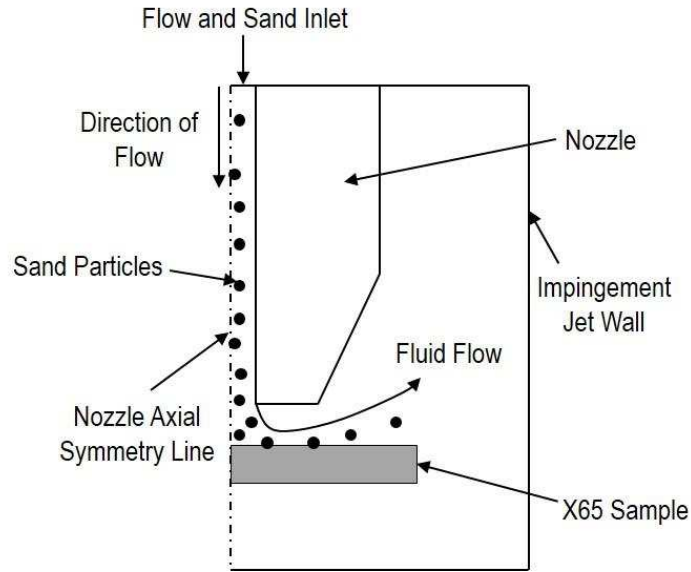
Figure 4: Simplified SIJ nozzle geometry used in the CFD model, demonstrating sand particle flow through the nozzle and impingement onto the target specimen

Once the fluid flow model was solved, particle trajectories were predicted. The Lagrangian approach was used due to the low sand concentration and small sized particles [34]. The following equation of particle motion, based on Newton's laws of motion, was used [35]:

$$m_p \frac{dV_p}{dt} = F_d + F_p + F_b + F_a \tag{8}$$

where m_p is the mass of the particle, dV_p/dt is the rate of change in particle velocity. The forces on the right-hand side of the equation consist of a drag force, F_d, the force due to the pressure gradient, F_p, the buoyancy force, F_b, and the force due to the added mass of the particle, F_a. This equation, the equations used to calculate the individual forces in the equation and the assumptions used in CFD particle tracking models have been defined previously [31, 36, 37]. A detailed description of the particle tracking model is provided as Supplementary Material.

The experimental conditions stated previously were modelled to predict the impact angles, number of impacts and impact velocities. To replicate a solution temperature of 60°C, a density of 983.2 kg/m³ and dynamic viscosity of 4.67 x 10⁻⁴ Pa.s was used to define the fluid conditions [38]. Spherical particles of a diameter of 250 µm were modelled through the SIJ nozzle. A total of 50,000 particles were released through the nozzle in the model, to give a good statistical range of impact angles and impact velocities on the sample surface. The particle trajectories predicted in the SIJ nozzle flow using CFD are shown in Figure 5. A

stagnation region was observed in the centre of the sample with higher velocities predicted in the turbulent jet region as the flow spreads. A wide range of particle impact angles from 0° to 90° and particle impact velocities were predicted on the surface in Figure 6, with most of the impacts occurring within 3 mm from the centre of the sample. Similar predictions of impact angle and impact velocity across the sample surface were made by Gnanavelu et al. [29], but their predictions showed that particles would impact over a much larger surface area due to the larger diameter nozzle used.
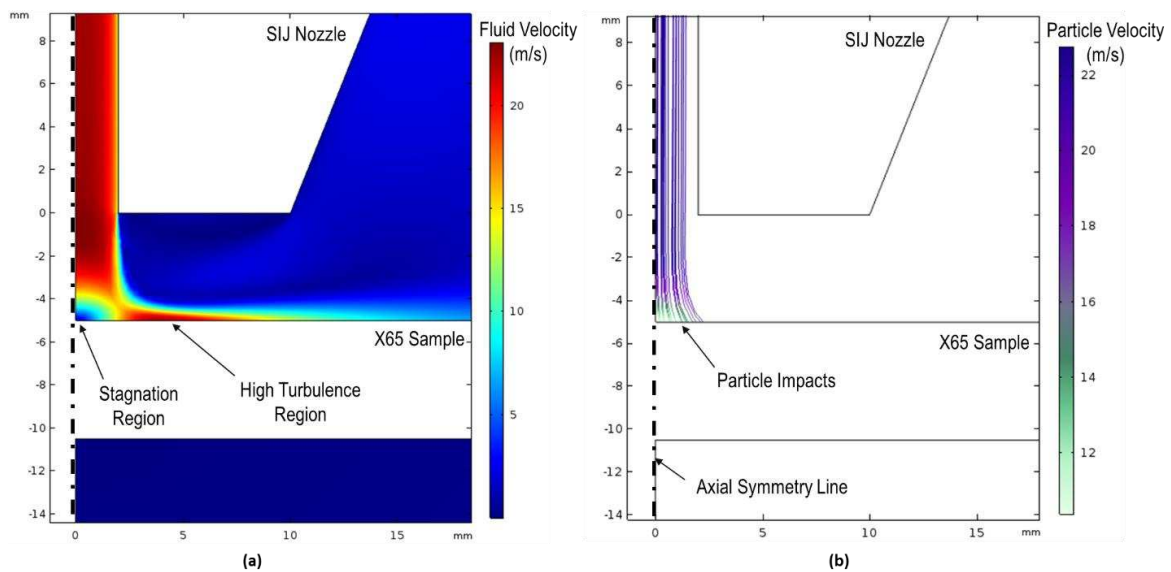

Figure 5: CFD prediction of (a) fluid flow through the SIJ nozzle and (b) trajectories of 250 μm diameter sand particles through the 4 mm diameter SIJ nozzle, positioned 5 mm from the sample, at a flow velocity of 20 m/s and temperature of 60°C
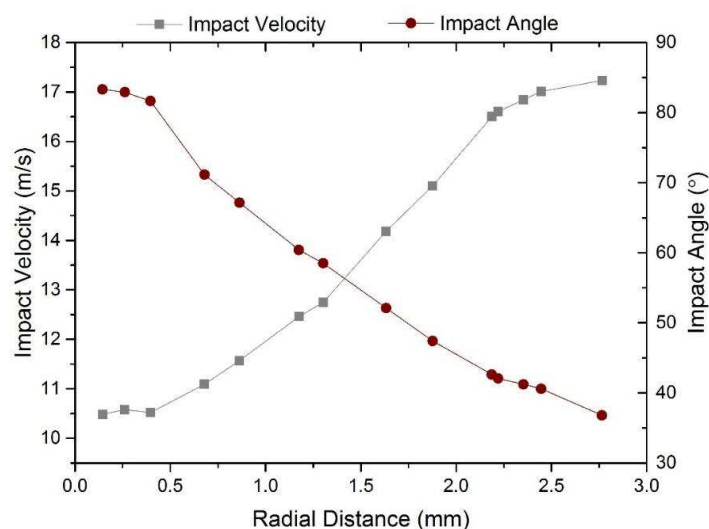

Figure 6: Impact angles and impact velocities of 250 μm diameter sand particles predicted across the surface of the sample positioned 5mm from a 4 mm diameter SIJ nozzle at a flow velocity of 20 m/s and temperature of 60°C

4. Results & Discussion

4.1. Definition of Impact Regions on Surface

Different regions were identified on the surface of the sample to understand how particle impact angles and particle impact velocities affected the surface of samples after erosion and erosion-corrosion tests. A 3D profile of the surface of a carbon steel sample was measured after a 240-minute erosion-corrosion SIJ test, using a Bruker NPFLEX white light interferometer. A 2D profile was extracted through the centre of the wear scar from the 3D profile and combined with the predictions of impact angle and impact velocity to identify different regions on the sample in Figure 7. Region 1 covered the width of the stagnation point and experienced high particle impact angles at relatively lower velocities. In this region, most of the erosion wear was expected to be in the form of plastic deformation due to indentation from the particles at high impact angles [13]. Region 2 showed increased flow velocities, compared to region 1, with high impact angles. Region 3 showed a highly turbulent region, with cutting wear from particle impacts expected due to lower impact angles [13]. Region 4 was expected to have very few particle impacts.
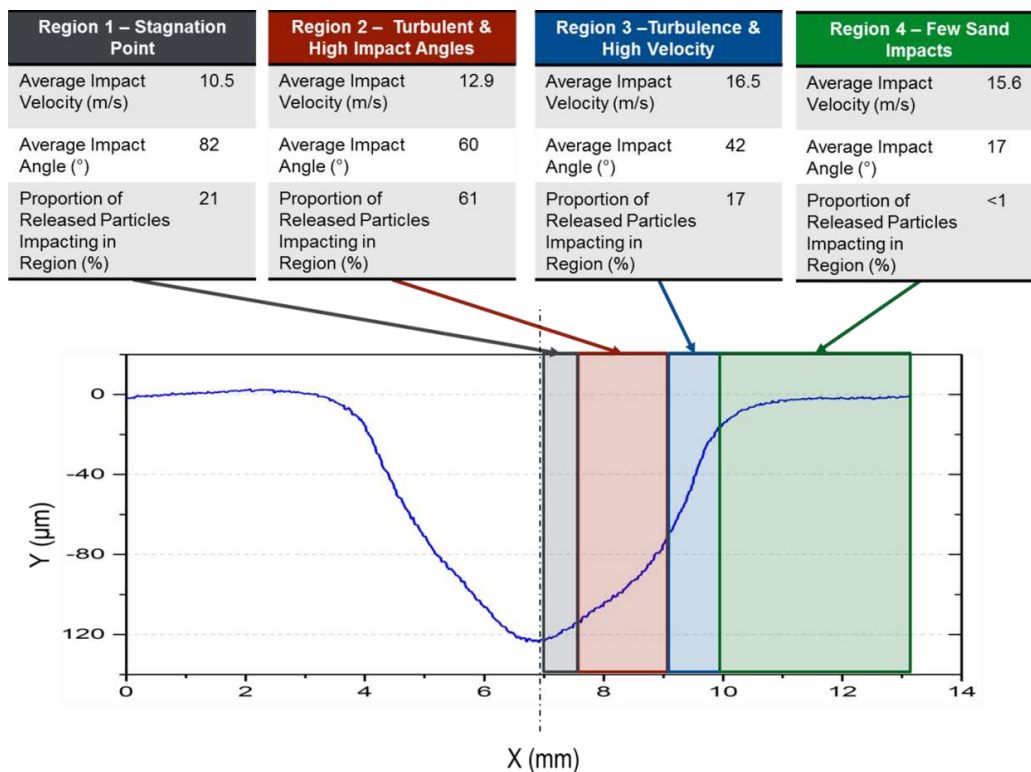

Figure 7: Identification of four regions on the profile of an X65 sample after a 240-minute erosion-corrosion test at 20 m/s, 60°C with 1000 mg/L of sand showing different particle impingement conditions in each of the regions predicted using CFD

4.2. Erosion-Corrosion SIJ Tests

Flow-induced corrosion, erosion and erosion-corrosion mass loss tests using the SIJ were completed. Figure 8 shows that each of the contributing parameters to total erosion-corrosion degradation increased linearly with time, indicating a constant degradation rate throughout the test. Average mass loss is reported from four carbon steel specimens, with error bars representing the standard deviation. The contributions of erosion and corrosion to total erosion-corrosion degradation were similar throughout the test period in these conditions, and there was a significant contribution of corrosion-enhanced erosion.
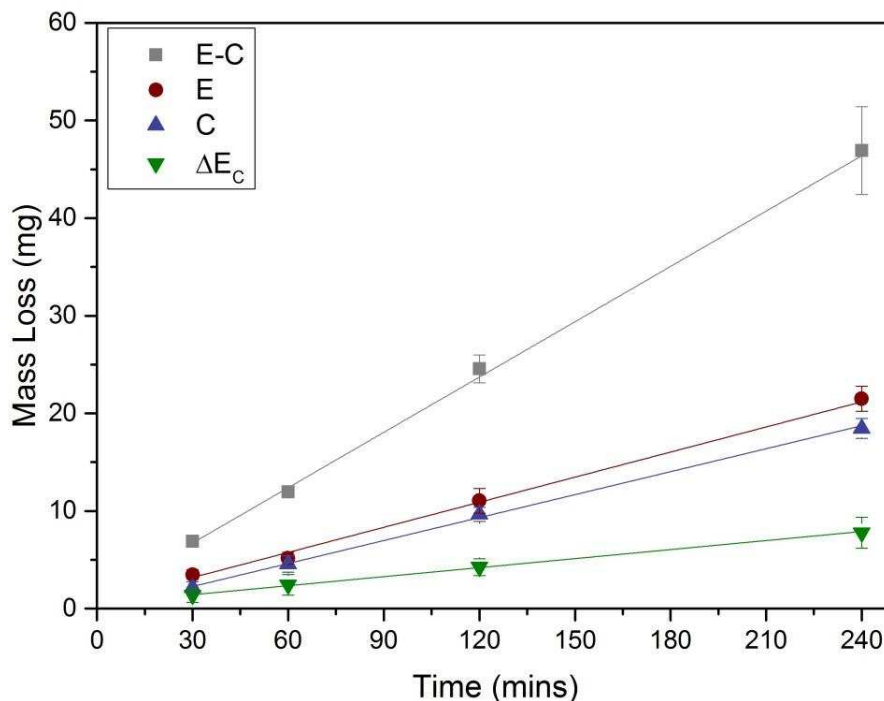

Figure 8: Components of total erosion-corrosion degradation of X65 carbon steel in SIJ tests at a flow velocity of 20 m/s in a 60°C solution where 'E-C' is erosion-corrosion degradation in CO_2-saturated, 2% NaCl conditions containing 1000 mg/L of sand; 'E' is pure erosion in N_2-saturated conditions containing 1000 mg/L of sand; 'C' is flow-induced corrosion in CO_2-saturated, 2% NaCl conditions and 'ΔE_C' is corrosion-enhanced erosion determined using Equation (1)

The corrosion rates calculated using EIS measurements to determine charge-transfer resistances and potentiodynamic sweeps to determine Tafel constants, for erosion-corrosion and flow-induced corrosion conditions are compared in Figure 9. Two repeats of electrochemistry measurements were completed in both conditions. Higher corrosion rates were observed during the first 10 – 20 minutes, as a result of a settling period in the SIJ as conditions reached consistency throughout the solution shortly after starting the test.

14

Conditions were maintained during the test, therefore corrosion rates remained constant, as shown in Figure 8 and Figure 9.

A slight increase in corrosion rate was observed during the test in erosion-corrosion conditions, but the change was not significant enough to conclude that corrosion was enhanced by erosion. A very small change in the corrosion rate in erosion-corrosion conditions (< 1 mm/yr) was measured. Compared to the significance of error in this measurement, the erosion-enhanced corrosion over a 240-minute period would be insignificant in comparison to the overall degradation rates measured in the tests shown in Figure 8. Longer term tests may have shown that this increase could become significant, but due to the constantly changing geometry of the sample, and increasing surface area, from mechanical degradation during the test and potential degradation of sand particles, the conditions during longer term tests could change significantly from the tests completed over a 240-minute period, making a direct comparison between results difficult. Therefore, it was assumed that erosion-enhanced corrosion was negligible for the comparison in these tests.
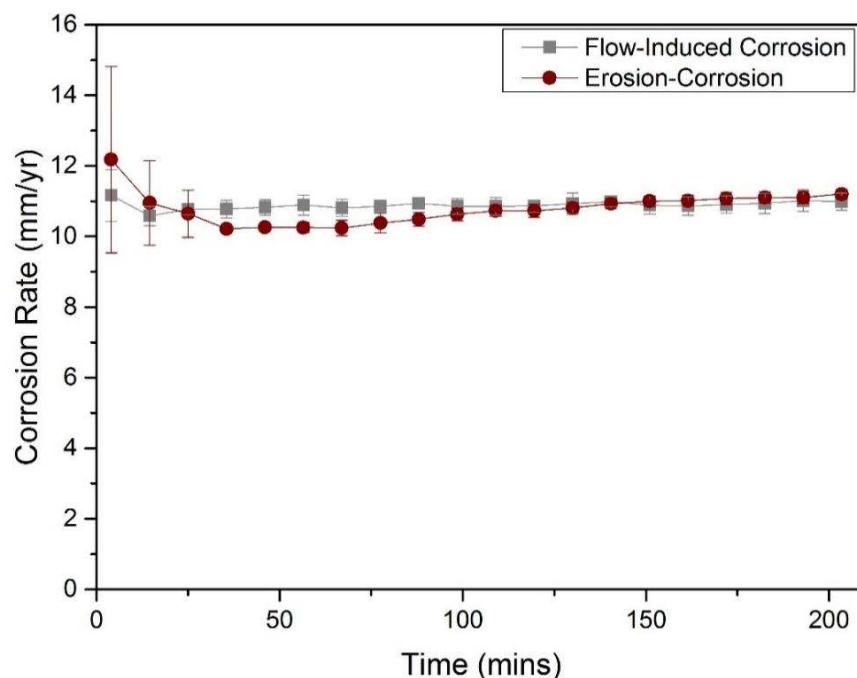
Figure 9: Comparison of in-situ corrosion rates calculated using EIS measurements to determine charge-transfer resistance and Tafel constants determined from potentiodynamic sweeps in flow-induced corrosion SIJ tests at 20 m/s in a 2% NaCl, 60°C solution and erosion-corrosion tests containing 1000 mg/L of sand

The Tafel constants used to calculate the corrosion rates in Figure 9 were determined using the Tafel plots in Figure 10 at a potential of OCP ± 50mV, with a Stern-Geary coefficient of

28.5 for erosion-corrosion tests and 26.9 calculated for flow-induced corrosion tests. These Stern-Geary coefficients were assumed to be constant throughout the 240-minute experiments, as corrosion rates from mass loss and electrochemistry measurements were shown to be constant throughout the test duration. The flow-induced corrosion Stern-Geary coefficient agreed with mass loss measurements. Mass loss rates of 4.58 mg/hr $\pm$ 0.18 mg/hr were measured in flow induced corrosion conditions and converted to corrosion rates using Equation (7), giving corrosion rates of 10.4 mm/yr $\pm$ 0.4 mm/yr, less than 5% lower than average electrochemistry measured corrosion rates.

The contribution of each degradation mechanism to total erosion-corrosion degradation is shown in Figure 11. The most significant enhanced effect was corrosion enhanced erosion, accounting for approximately 15-20% of total erosion-corrosion wear. Proportionally, erosion wear accounted for a smaller contribution to total erosion-corrosion degradation from 30-minutes onwards, dropping from approximately 50% to 43-45%.
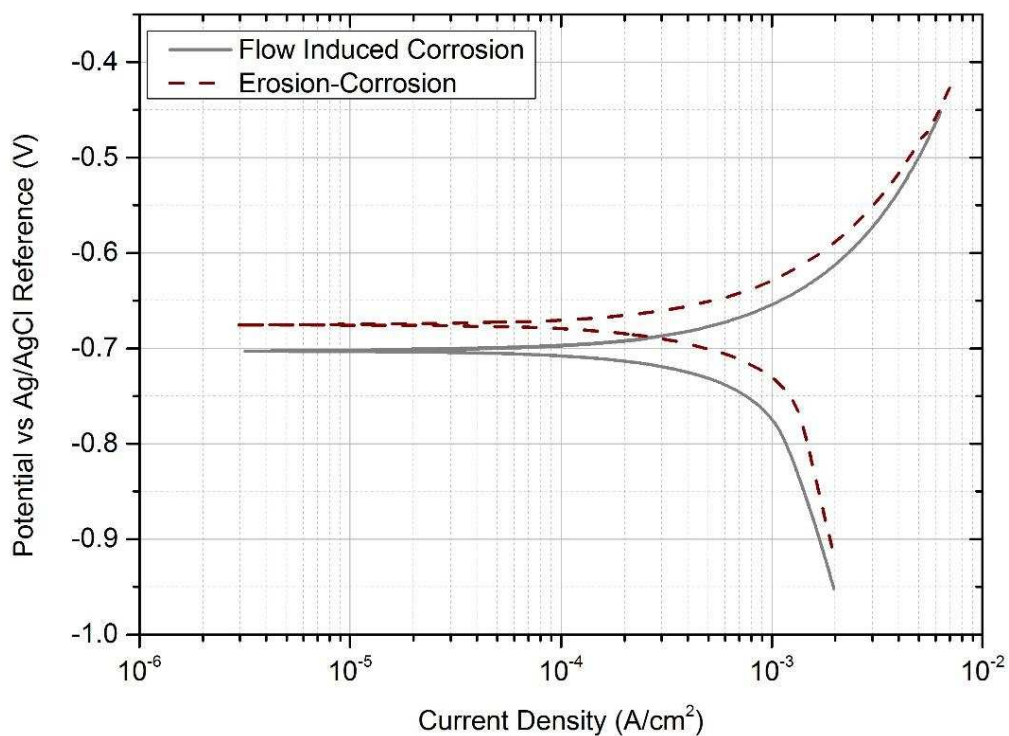

Figure 10: Tafel plots of X65 carbon steel used to obtain Tafel constants measured after 210 minutes in flow-induced corrosion SIJ tests at a flow velocity of 20 m/s in a 2% NaCl solution at 60°C and erosion-corrosion tests containing 1000 mg/L of sand
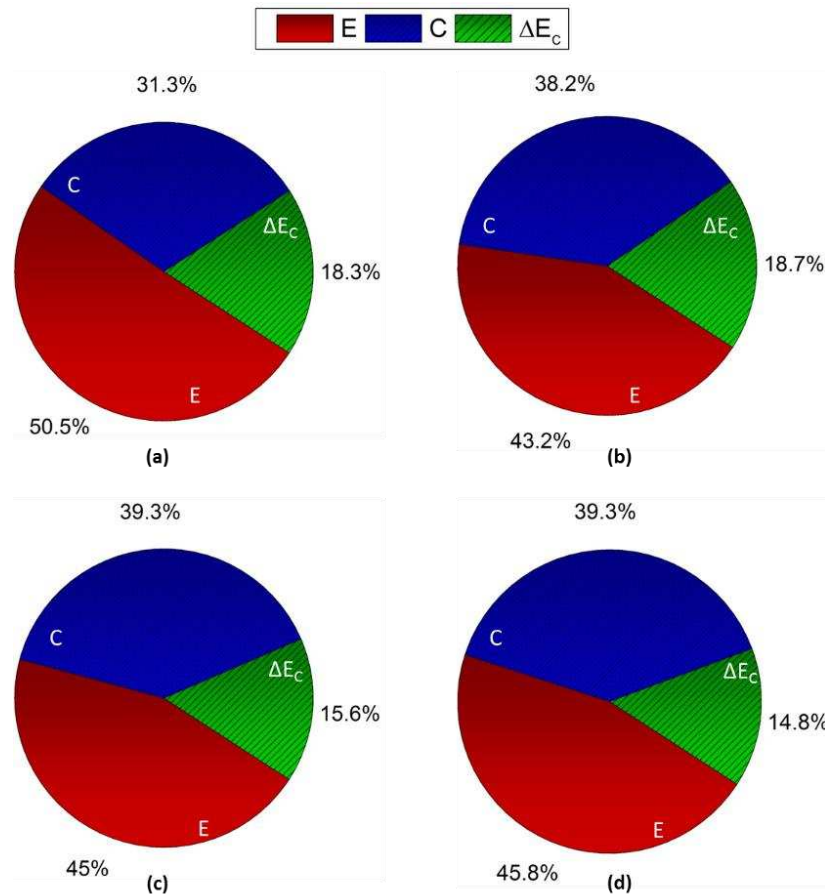
Figure 11: Contributions to total erosion-corrosion degradation of pure erosion in N_2-saturated conditions containing 1000 mg/L of sand (E), flow-induced corrosion in CO_2-saturated conditions (C) and corrosion-enhanced erosion in CO_2-saturated conditions containing 1000 mg/L of sand (ΔE_C) in (a) 30-minute, (b) 60-minute, (c) 120-minute and (d) 240-minute SIJ tests at 20 m/s in a 60°C solution

4.3. Surface Analysis

Surface profiles of the samples were measured using a Bruker NPFLEX white light interferometer. 3D profiles were measured over the entire surface of the samples after erosion-corrosion and erosion tests, with 2D profiles extracted from the 3D profile to compare wear depth between the samples. Two erosion and two erosion-corrosion wear profiles after a 240-minute test period are compared in Figure 12. The 2D profiles, extracted from the 3D profiles, were shown through the centre of the wear scars on each of the samples, where the penetration depth was at a maximum on the surface. A 'U-shaped' wear scar was observed, as opposed to the typical 'W-shaped' scar typically observed in SIJ erosion testing, where degradation is significantly lower in the centre stagnation region on the sample [29, 30]. However, at flow velocities of 20 m/s a 'U-shaped' wear scar has been observed

17

previously, similar to the wear scar measured in Figure 12 [10]. Gnanavelu et al. [29] measured a 'W-shaped' wear scar, but impact velocities of approximately 1 m/s were predicted using CFD in the stagnation region on the sample, significantly lower than the predicted impact velocities in the stagnation region shown in Figure 6.
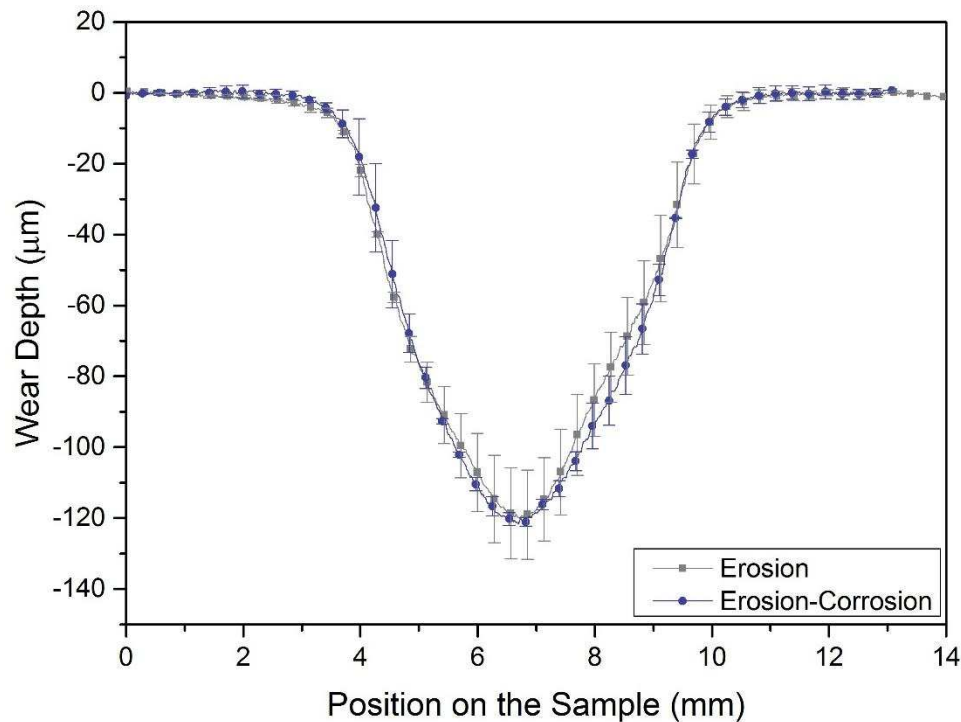

Figure 12: 2D profiles of X65 carbon steel surfaces after 240-minute SIJ erosion and erosion-corrosion tests at a flow velocity of 20 m/s in a 60°C solution containing 1000 mg/L of sand

In the central stagnation region (region 1), the particle trajectories did not deviate significantly despite the decrease in fluid flow velocity, resulting in high quantities of particle impacts. High particle equilibration numbers were expected in the conditions tested, as a result of the particle size and low fluid viscosity, meaning that the particles were highly likely to deviate from fluid streamlines [39]. This therefore explained why large quantities of particle impacts were observed in the centre of the sample, and why particle velocities and particle impact angles were not significantly reduced in the stagnation region (region 1). In region 2 and region 3, the turbulent jet region, high rates of degradation were observed. Higher turbulence in these regions caused increased particle velocities and spreading of the flow radially reduced particle impingement angles. Fewer particles, however, were predicted to impact the surface in region 3, therefore, explaining why wear depth was reduced in this region compared to region 1 and region 2. As flow spreads radially towards the edge of the

sample in region 4 there were fewer particle impacts. Due to the high particle equilibration number, the majority of particles had impacted on the surface in regions 1 - 3.

The profiles shown in Figure 12 also partially validate the predictions of the CFD model, as no significant wear was observed towards the edge of the sample, outside of the wear scar, with the width of the wear scar being approximately 6 mm in diameter. This was shown in the CFD model, where the majority of the particle impacts occurred within a radial distance of 3 mm from the centre of the sample.

The effects of erosion and erosion-corrosion degradation on the surface of samples after testing was analysed using SEM. SEM images of each of the regions in Figure 13 of erosion and erosion-corrosion samples after 240 minutes confirmed that high amounts of plastic deformation occurred in region 1 due to high impact angles. Several impact zones could be seen in this region on both erosion and erosion-corrosion samples. In region 2 and region 3 more cuts could be seen on the surface due to the low impact angle of the sand particles, with the surfaces of the samples visibly rougher in these regions. Region 4 showed no impacts on the surface in the regions analysed. Similar surfaces were observed between erosion and erosion-corrosion samples in each of the four regions. These SEM images also added further support to the validity of the CFD model, as the mechanisms of wear for the predicted impact angles and impact velocities in each of the four regions agreed with the typical mechanisms of wear expected for those impact conditions.
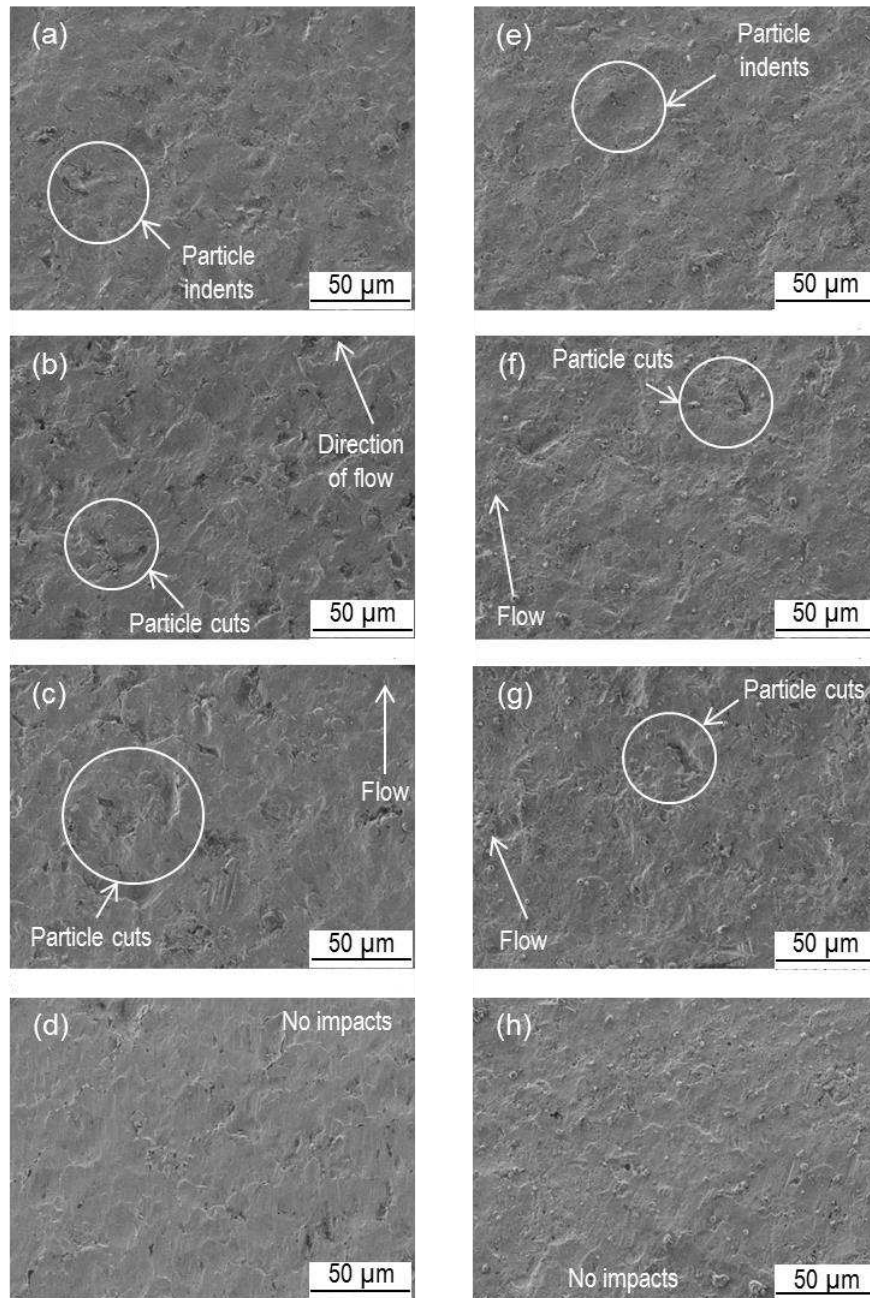
Figure 13: SEM images of erosion (a-d) and erosion-corrosion (e-h) samples after 240-minute tests in the SIJ at a flow velocity of 20 m/s in a solution at a temperature of 60°C containing 1000 mg/L of sand in region 1 (a,e), region 2 (b,f), region 3 (c,g) and region 4 (d,h)

Surface roughness (S_a) of the sample in each of the four regions was measured using the NPFLEX 3D surface profiler with a 0.8 mm Gaussian cut-off filter. Changes in surface roughness were observed in each of the regions for erosion tests as shown in Figure 14, showing the average surface roughness and standard deviation from four samples. Surface roughness was highest in region 3 where high levels of cutting were experienced as predicted

by the CFD model and impact angles were in the range of 40°-50°. It has been reported that surface roughening is highest at impact angles between 40° and 60° [13]. Region 2 also showed a higher surface roughness compared to region 1, therefore suggesting that material removal due to cutting mechanisms produce a rougher surface after erosion testing. Impact velocity was also predicted to be highest in region 3, potentially contributing to the increased surface roughness in this region. High rates of plastic deformation in region 1 caused some increase in surface roughness, but this was not as significant as the surface roughness increase in regions where cutting was the main mechanism of wear. Similar values of surface roughness were measured on erosion and erosion-corrosion samples in regions 1, 2 and 4, as shown in Figure 14. A slightly higher surface roughness was observed on the erosion-corrosion samples in region 3 but there was no obvious reason for this difference.
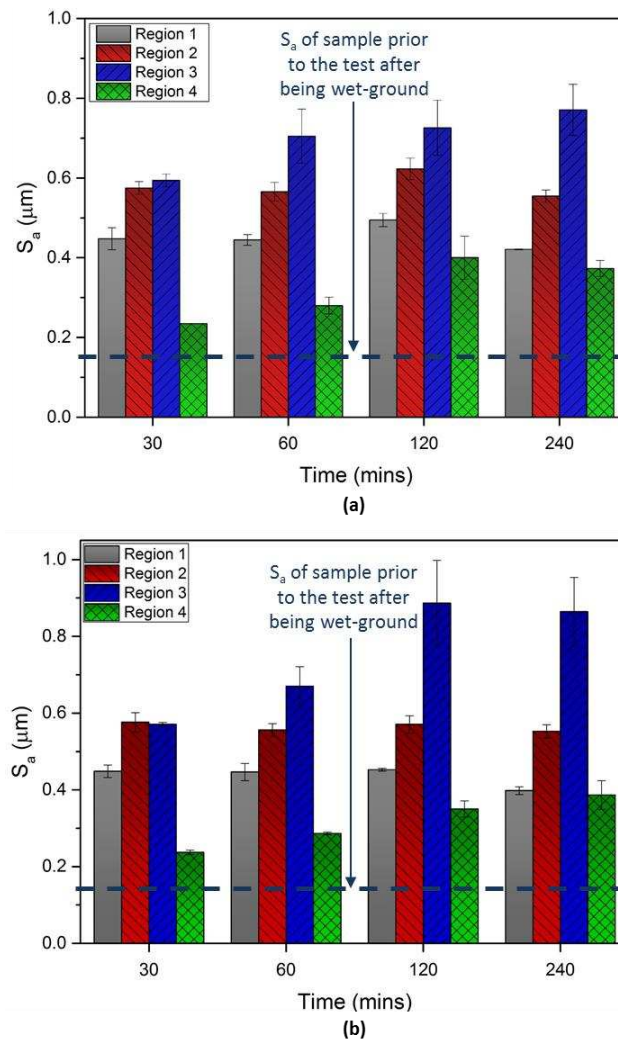

Figure 14: Measurement of surface roughness (S_a) on the surface of X65 samples after (a) pure erosion SIJ tests in N_2 saturated conditions and (b) erosion-corrosion SIJ tests at 20 m/s and 60°C solution containing 1000 mg/L of sand

Despite the increase in surface roughness on the samples, the corrosion rate was not significantly affected, suggesting the effect of erosion-enhanced corrosion is not a significant issue for carbon steel when no surface films are present. There was also no significant change in surface roughness over time, suggesting that surface roughening did not contribute to the slight increase in in-situ corrosion rate measured in Figure 9. The increase in surface area of the samples as a result of the change in surface profile after 240 minutes of particle impacts in both erosion and erosion-corrosion conditions was measured to be less than 0.1% from the 3D profiles obtained using the NPFLEX. This calculation of surface area also accounted for the increase in surface roughness, showing that change in surface area had a negligible effect on corrosion rates.

4.4. Analysis of Work Hardened Layers

Hardness of the X65 samples was compared after each of the erosion and erosion-corrosion tests using a micro indenter. Vickers hardness (H_V) was measured at multiple points along the surface, through the centre line of the wear scar. Two samples for each test condition were indented, with an average from a minimum of six indentations reported in each region on the surface. Strain hardening was expected due to the repeated impacts of sand particles on the surface of the samples and this was seen in regions 1-3 after erosion tests, shown in Figure 15. It was observed that there was no influence of particle impact angle and impact velocity on work hardening of the sample, with hardness being approximately the same in each of the three impact regions, despite CFD predictions showing that impact angle and impact velocity would vary in each of the regions. It has also been shown previously in measurements of micro-hardness after SIJ tests that hardness is approximately constant over the width of wear scars, suggesting that work hardening mechanisms are not significantly dependent upon particle impact angle in SIJ conditions [7, 19]. The hardness in region 4 was much lower where there were significantly fewer particle impacts.

The average hardness in regions 1-3 was similar between erosion and erosion-corrosion samples. It was expected that the surfaces of erosion samples would be harder, with corrosion of the work hardened layers reducing the hardness of the samples in erosion-corrosion tests, but the difference was not significant. The difference in hardness between erosion and erosion-corrosion samples was most significant after 30 minutes, which

correlated with the results in Figure 8, where corrosion-enhanced erosion accounted for a slightly greater proportion of erosion-corrosion wear in the first 30 minutes.

Figure 15: Measurement of Vickers hardness (H_V) on the surface of the sample after (a) pure erosion tests in N_2 saturated conditions and (b) erosion-corrosion tests in CO_2-saturated conditions at 20 m/s and 60°C solution containing 1000 mg/L of sand

Naim and Badahur [40] showed how hardness increased after only a few impacts before reaching a constant value where no further increase in hardness was observed despite continued particle impacts. This was conducted using much larger diameter particles and on a different material than was used in the SIJ tests in this paper; however, the surface of the carbon steel samples also appeared to harden at a very fast rate before reaching a maximum value, as no significant difference was observed between measurements of hardness completed after 30 minutes and 240 minutes. 1, 5 and 10-minute erosion tests were

completed to investigate the rate of work hardening of the samples in the same erosion conditions as previous tests at 20 m/s with 1000 mg/L of sand, with the results provided in Figure 16. Average hardness measurements in regions 1 - 3 are reported, with the error bars representing standard deviation. A significant increase in hardness was measured after 1 minute, before reaching a peak hardness after approximately 10 minutes. At this point no significant increase in hardness was observed despite high quantities of particle impacts, explaining why erosion rates remained relatively constant in the measurements from 30 minutes to 240 minutes, as shown in Figure 8. The corrosion effect on the work hardened layers is also shown in Figure 16. Corrosion tests were completed on samples that were work hardened in pure erosion conditions for a period of 120 minutes prior to the test. The aim of this was to measure the reduction in hardness of the samples as a result of corrosion of the work hardened layers. Corrosion tests were completed in the same conditions as the previous corrosion tests at a flow velocity of 20 m/s in the SIJ. The hardness of the samples was reduced, but the rate of removal was much lower than the rate of work hardening in erosion conditions. The hardness was not reduced to the original value of hardness measured prior to work hardening and the hardness appeared to reach a constant value from 10-30 minutes, with the rate of work hardening much greater than the rate of removal of work hardened layers by corrosion.
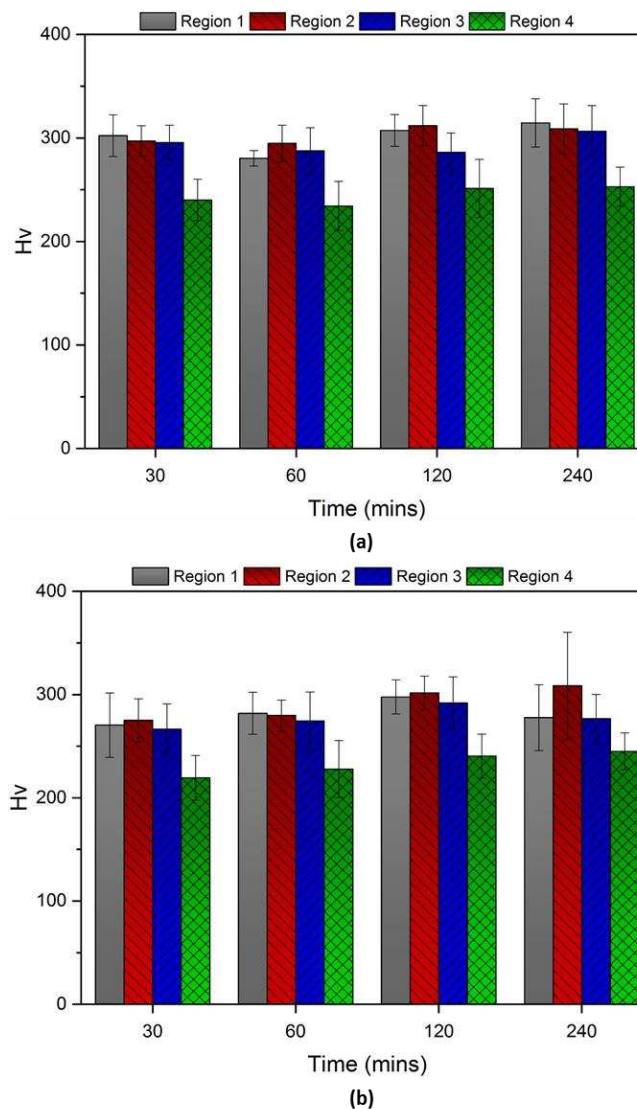

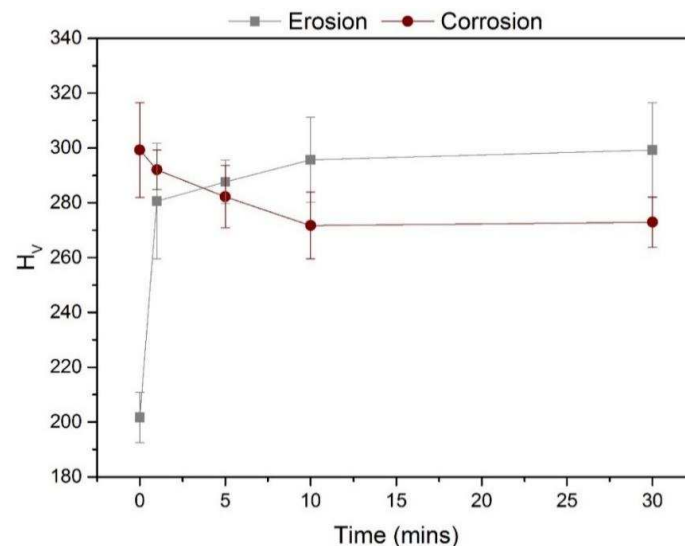**Figure 16: Measurement of Vickers hardness (H_V) on the surface of X65 samples after pure erosion SIJ tests in N_2-saturated conditions in a 60°C solution containing 1000 mg/L of sand and removal of work hardened layers from previously work hardened samples in flow-induced corrosion SIJ tests at a flow velocity 20 m/s in a 2% NaCl, 60°C, CO_2-saturated conditions**

Work hardened layers were analysed to compare the effects of work hardening on the microstructure of X65 samples after erosion and erosion-corrosion tests by completing FIB-SEM analysis. No obvious significant differences between the erosion and erosion-corrosion samples were observed up to this point, in terms of measured surface roughness and hardness that would explain the cause of interactions, therefore analysis of the subsurface was required. An X65 sample was analysed prior to testing after being wet-ground, shown in Figure 17, to compare the subsurface of an untested sample with the samples used in erosion and erosion-corrosion tests. A thin region of grain refinement, approximately 1 µm thick, was observed as a result of the wet grinding process. Larger grains were observed beneath this layer of grain refinement, typical of the bulk grains expected in the X65 microstructure.
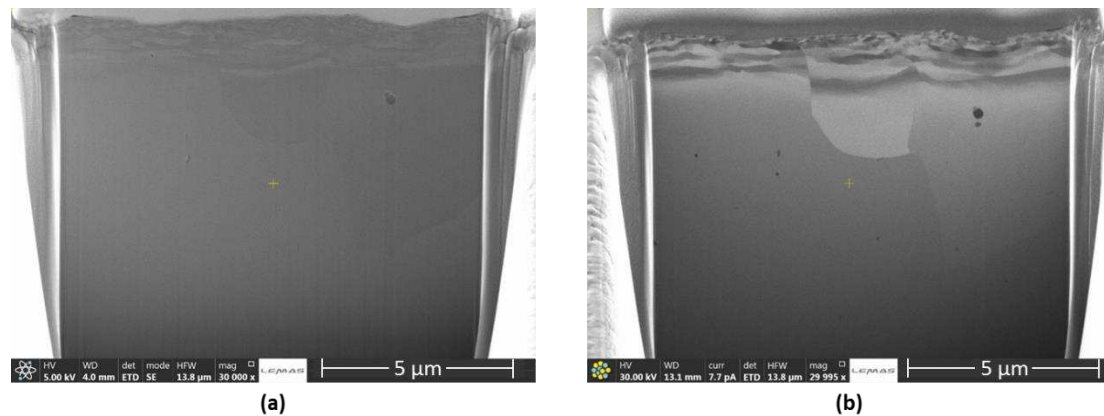

Figure 17: Cross sections in the centre of an X65 sample prior to SIJ testing wet-ground to a surface finish of 0.15 µm ± 0.02 µm milled using FIB and imaged using (a) SEM at 30,000x magnification and (b) FIB etching

Four test samples were analysed using the FIB-SEM to compare erosion and erosion-corrosion effects on the microstructure. Erosion samples after 30 minutes and 240 minutes of testing were compared with erosion-corrosion samples after the same test duration. A small region in the centre of the wear scar on each of the samples was milled and analysed using the FIB. The microstructures of the four samples are shown in Figure 18. Compared with the FIB images of the sample prior to testing, in Figure 17, grain refinement was observed in the microstructure of each of the four samples analysed after testing. Two distinct regions of grain refinement were observed, with a very fine grain structure closest to the surface and slightly larger grains beneath. The work hardened layer closest to the surface, consisting of nano-grains and approximately 1 µm thick, was present closest to the surfaces of all samples. Underneath the nano-grain layer, grain refinement was still observed but the grains were

slightly larger in size. Large grains, similar in size to the grains observed in the bulk of the sample prior to testing, were present beneath these two refined layers, with some deformation of the bulk grains observed. Similar layers were observed by Rajahram et al. [20] from FIB analysis of UNS S31603 after erosion-corrosion tests, where it was suggested that nano-grains were formed closest to the surface due to the kinetic energy of initial particle impacts. Subsequent particle impacts in the work hardened region resulted in load being transmitted to bulk grains, causing micro-grains to form beneath the nano-grain layer and eventually deformation of the bulk grains [20].

The thickness of both the nano-grain layer and micro-grain sublayer increased over time on the erosion samples, with the increase in the micro-grain sublayer much more significant than the nano-grain layer thickness increase. Overall work hardened layers were thicker on erosion samples than erosion-corrosion samples. This was most obvious in the comparison between the samples after 240-minutes, where nano-grain layers were slightly thicker and micro-grain layers were significantly thicker on the erosion sample. Nano-grains also appeared to be more refined on the erosion samples than on the erosion-corrosion samples. The corrosion of nano-grain layers continuously exposed softer material, by removing nano-grain layers closest to the surface. However, nano-grain layers were still observed on erosion-corrosion samples, therefore suggesting the nano-grain layer formed at very high rates and that only a few particle impacts were required to generate the layer. The high rates of work hardening in the high flow velocity and sand concentration used in this work, shown previously in Figure 16, also supported this observation. However, the continuous removal of nano-grain layers because of corrosion mechanisms meant that micro-grain layers were not as thick, probably due to fewer particle impacts in the same locations on the surface, meaning load from particle impacts was not transferred to bulk grains beneath the nano-grain layer to the same extent as erosion samples, where less overall material removal occurred.
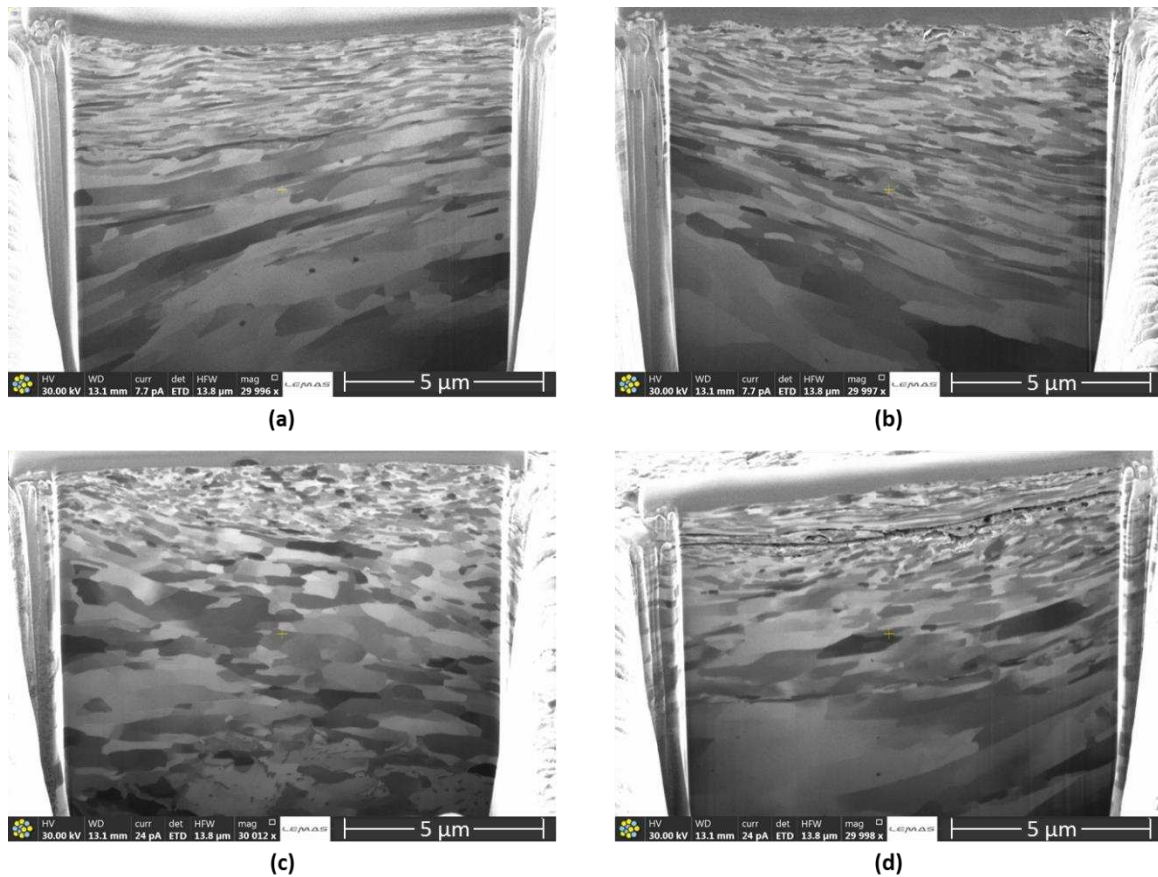
Figure 18: FIB images of cross sections measured after (a) 30-minute erosion tests, (b) 30-minute erosion-corrosion tests, (c) 240-minute erosion tests and (d) 240-minute erosion-corrosion tests in the centre of region 1 on the samples

The presence of a thick micro-grain layer on erosion samples also explained why the corrosion of the work hardened layers above did not reduce sample hardness to pre-test levels, shown in Figure 16. An approximate corrosion mass loss rate of 4.59 mg/hr ± 0.38 mg/hr was measured, which, if assumed to be constant over the surface of the sample, was equivalent to a thickness loss of 1.24 μm/hr ± 0.10 μm/hr. Therefore, in a 30-minute period, it was estimated that approximately 0.6 - 0.7 μm of material would have been removed, meaning that some of the nano-grain layer probably remained, with the micro-grain layer beneath remaining in full. The lack of a thick micro-grain layer on erosion-corrosion samples could have potentially contributed to erosion-enhanced corrosion as softer grains underneath this layer were more likely to be exposed after corrosion.

SEM images of the cross sections milled by the FIB are shown in Figure 19. Several voids were observed on the erosion-corrosion samples that were not observed to the same extent on the erosion samples, thought to be subsurface cracks. Some very fine cracks were also present

on the surface of the erosion samples, but these cracks had not propagated further into the material. It should be noted that FIB analysis is completed on a very small scale and it could be argued that the large voids on the surface were observed because of overlapping material such as lips formed from particle impacts close to the region analysed. However, smaller cracks were also observed that initiated within the region of the milled area and the cracks did appear to be similar to the subsurface FIB analysis completed by Rajahram et al. [41] after erosion-corrosion tests where micro-cracks and nano-cracks were observed.
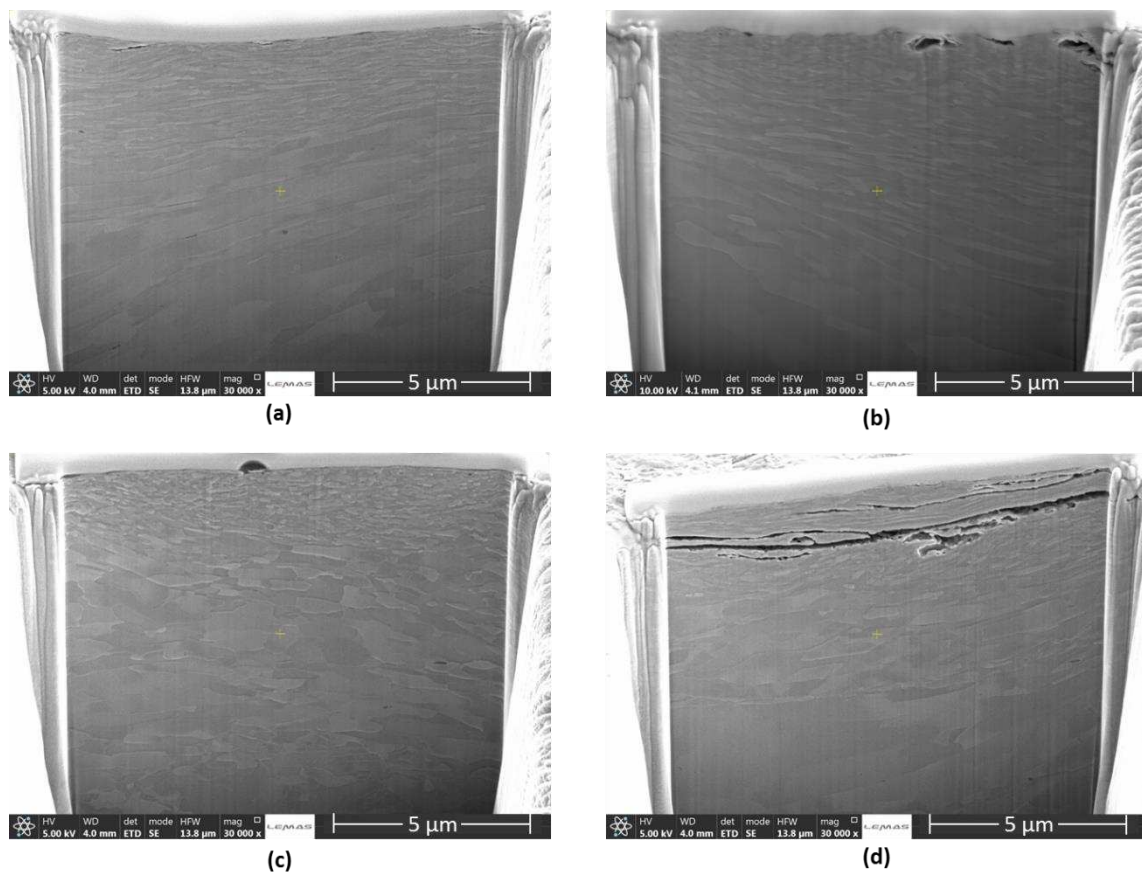
Figure 19: FIB-SEM images of cross sections measured after (a) 30-minute erosion tests, (b) 30-minute erosion-corrosion tests, (c) 240-minute erosion tests and (d) 240-minute erosion-corrosion tests in the centre of region 1 on the samples

Several theories exist that explain subsurface cracking of steels as a result of particle impacts. Levy [23] observed subsurface cracks on pearlitic carbon steels used in particle impact testing, thought to be due to fracture of brittle cementite regions after particle impacts. Repeated impacts and the formation of nano-grains can also cause the nano-grain layer to become brittle [18]. The erosion behaviour of ductile materials and brittle materials vary significantly, with high impact angles causing the highest rates of wear of brittle materials [16]. The impact

28

of particles on brittle materials can cause fracture, where material is removed by the formation and intersection of cracks [42]. This could also potentially explain why 'U-shaped' wear scars were observed in Figure 12, with impact angles predicted to be approximately 90° in the central stagnation region (region 1), as degradation rates for brittle materials are expected to be highest at impact angles of 90°. This potentially explains why most degradation was measured in the centre of the wear, due to the high rates of work hardening and resulting embrittlement of the surface in this region. Jiang et al. [27] also suggested that repeated impacts on the surface caused low cycle fatigue cracking with the initiation of cracks caused at lips formed from impact craters after particle indents as shown by Rajahram et al. [41].

Large cracks were not observed on the erosion sample after 240 minutes in Figure 19, but were observed on the erosion-corrosion sample. It is possible that in the region analysed on the erosion sample, cracks were not present but could have been present in other areas. However, there are several potential reasons why cracks could be present on the erosion-corrosion sample but were not on erosion samples. The corrosion mechanisms could have accelerated the growth of the crack, meaning that any cracks on erosion samples would not have propagated at the same rate [26]. Cracks were only observed in the nano-grain region and in the region of the transition between the nano-grain layer and the micro-grain sublayer, where embrittlement was most likely to be expected, due to the very fine grain structure. The growth of cracks could potentially loosen the material between the grain boundaries, therefore enhancing the material damage as a result of particle impacts, and contributing to corrosion-enhanced erosion. However, the understanding of these mechanisms in erosion mechanisms does require further work to fully understand the mechanisms of subsurface degradation.

5. Conclusion

Erosion-enhanced corrosion and corrosion-enhanced erosion processes were analysed on X65 carbon steel surfaces after erosion-corrosion, flow-induced corrosion and erosion tests using the SIJ. Using CFD to develop a model to predict the trajectories of sand particles

through an SIJ nozzle, a range of surface analysis techniques and measurements of degradation rates in SIJ tests, the following conclusions were reached:

- All contributing factors to total erosion-corrosion degradation occurred at a constant rate, with a steady linear increase seen in erosion, corrosion, erosion-corrosion and corrosion-enhanced erosion over the test period of 240 minutes.

- Erosion-enhanced corrosion was not a significant contributing factor, despite the significant increase in surface roughness across the wear scar of the sample. Corrosion rates measured during erosion-corrosion tests did increase slightly during a 240-minute period, but this was not significant relative to the total erosion-corrosion degradation rates.

- Corrosion-enhanced erosion was the most significant enhancement of erosion-corrosion wear. Corrosion of work hardened layers and subsequent hardening of the sample at high rates continuously exposed softer areas of material and prevented thick work hardened layers from forming.

- A range of impact angles from approximately 30° - 90° and impact velocities from approximately 10 – 17 m/s were predicted using CFD on the surface of the sample in SIJ erosion and erosion-corrosion tests, with regions of different degradation mechanisms identified on the sample surface

- FIB-SEM images of the work hardened layers of erosion and erosion-corrosion showed a very refined nano-grain layer closest to the surface and a micro-grain layer beneath this layer. The nano-grain layers were more refined on erosion samples, and micro-grain layers were much thicker on erosion samples due to corrosion of work hardened layers in erosion-corrosion tests

- Cracks in the nano-grain layers were observed in the subsurface that were much more significant on erosion-corrosion samples than erosion samples, thought be due to corrosion mechanisms accelerating the growth of the crack. The initiation of the crack could have been caused by a low cycle fatigue mechanism, with corrosive species accelerating the growth of the crack

Acknowledgements

References

1. Burson-Thomas, C.B. and R.J. Wood, *Developments in Erosion–Corrosion Over the Past 10 Years.* Journal of Bio-and Tribo-Corrosion, 2017. **3**(2): p. 14.
2. Wood, R.J.K. and S.P. Hutton, *The synergistic effect of erosion and corrosion: trends in published results.* Wear, 1990. **140**(2): p. 387-394.
3. Barker, R., D. Burkle, T. Charpentier, H. Thompson, and A. Neville, *A review of iron carbonate (FeCO3) formation in the oil and gas industry.* Corrosion Science, 2018.
4. Tran, T., B. Brown, and S. Nesic, *Corrosion of mild steel in an aqueous CO_2 environment - basic electrochemical mechanisms revisited*, in *CORROSION 2015*. 2015, NACE International: Dallas, TX.
5. Bockris, J.M., D. Drazic, and A. Despic, *The electrode kinetics of the deposition and dissolution of iron.* Electrochimica Acta, 1961. **4**(2-4): p. 325-361.
6. Nešić, S., *Key issues related to modelling of internal corrosion of oil and gas pipelines – A review.* Corrosion Science, 2007. **49**(12): p. 4308-4338.
7. Aribo, S., R. Barker, X. Hu, and A. Neville, *Erosion–corrosion behaviour of lean duplex stainless steels in 3.5% NaCl solution.* Wear, 2013. **302**(1): p. 1602-1608.
8. Rajahram, S., T. Harvey, and R. Wood, *Full factorial investigation on the erosion–corrosion resistance of UNS S31603.* Tribology International, 2010. **43**(11): p. 2072-2083.
9. Rajahram, S.S., T.J. Harvey, and R.J.K. Wood, *Erosion–corrosion resistance of engineering materials in various test conditions.* Wear, 2009. **267**(1–4): p. 244-254.
10. Hu, X. and A. Neville, *CO_2 erosion–corrosion of pipeline steel (API X65) in oil and gas conditions - A systematic approach.* Wear, 2009. **267**(11): p. 2027-2032.
11. Islam, M.A. and Z. Farhat, *Erosion-corrosion mechanism and comparison of erosion-corrosion performance of API steels.* Wear, 2017. **376–377, Part A**: p. 533-541.
12. Wood, R.J.K., *Erosion–corrosion interactions and their effect on marine and offshore materials.* Wear, 2006. **261**(9): p. 1012-1023.
13. Bitter, J.G.A., *A study of erosion phenomena: Part II.* Wear, 1963. **6**(3): p. 169-190.
14. Alkhateeb, M., R. Barker, A. Neville, and H.M. Thompson, *The effect of surface roughness on diffusion and chemical reaction controlled limiting currents on a Rotating Cylinder Electrode in deaerated solutions with and without CO_2.* Corrosion, 2018.
15. Li, W. and D.Y. Li, *Influence of surface morphology on corrosion and electronic behavior.* Acta Materialia, 2006. **54**(2): p. 445-452.
16. Finnie, I., *Erosion of surfaces by solid particles.* Wear, 1960. **3**(2): p. 87-103.
17. Guo, H.X., B.T. Lu, and J.L. Luo, *Interaction of mechanical and electrochemical factors in erosion–corrosion of carbon steel.* Electrochimica Acta, 2005. **51**(2): p. 315-323.
18. Ashby, M.F. and D.R. Jones, *Engineering materials 1: an introduction to properties, applications and design*. 3rd ed. 2011, Oxford: Elsevier Butterworth-Heinmann.
19. Barik, R.C., J.A. Wharton, R.J.K. Wood, and K.R. Stokes, *Electro-mechanical interactions during erosion–corrosion.* Wear, 2009. **267**(11): p. 1900-1908.

20.   Rajahram, S.S., T.J. Harvey, J.C. Walker, S.C. Wang, R.J.K. Wood, and G. Lalev, *A study on the evolution of surface and subsurface wear of UNS S31603 during erosion–corrosion.* Wear, 2011. **271**(9–10): p. 1302-1313.

21.   Karlsson, B. and G. Lindén, *Plastic deformation of ferrite—pearlite structures in steel.* Materials Science and Engineering, 1975. **17**(2): p. 209-219.

22.   El-Danaf, E., M. Baig, A. Almajid, W. Alshalfan, M. Al-Mojil, and S. Al-Shahrani, *Mechanical, microstructure and texture characterization of API X65 steel.* Materials & Design, 2013. **47**: p. 529-538.

23.   Levy, A.V., *The solid particle erosion behavior of steel as a function of microstructure.* Wear, 1981. **68**(3): p. 269-287.

24.   Hutchings, I. and R. Winter, *The erosion of ductile metals by spherical particles.* Journal of Physics D: Applied Physics, 1975. **8**(1): p. 8.

25.   Finnie, I., *Some observations on the erosion of ductile metals.* Wear, 1972. **19**(1): p. 81-90.

26.   Jiang, J., M. Stack, and A. Neville, *Modelling the tribo-corrosion interaction in aqueous sliding conditions.* Tribology International, 2002. **35**(10): p. 669-679.

27.   Jiang, J., Y. Xie, M.A. Islam, and M. Stack, *The Effect of Dissolved Oxygen in Slurry on Erosion–Corrosion of En30B Steel.* Journal of Bio-and Tribo-Corrosion, 2017. **3**(4): p. 45.

28.   Oka, Y.I., M. Nishimura, K. Nagahashi, and M. Matsumura, *Control and evaluation of particle impact conditions in a sand erosion test facility.* Wear, 2001. **250**(1): p. 736-743.

29.   Gnanavelu, A., N. Kapur, A. Neville, and J.F. Flores, *An integrated methodology for predicting material wear rates due to erosion.* Wear, 2009. **267**(11): p. 1935-1944.

30.   Mansouri, A., H. Arabnejad, S.A. Shirazi, and B.S. McLaury, *A combined CFD/experimental methodology for erosion prediction.* Wear, 2015. **332–333**: p. 1090-1097.

31.   Chen, X., B.S. McLaury, and S.A. Shirazi, *Application and experimental validation of a computational fluid dynamics (CFD)-based erosion prediction model in elbows and plugged tees.* Computers & Fluids, 2004. **33**(10): p. 1251-1272.

32.   Senatore, E.V., W. Taleb, J. Owen, Y. Hua, J.A.C.P. Gomes, R. Barker, and A. Neville, *Evaluation of high shear inhibitor performance in CO2-containing flow-induced corrosion and erosion-corrosion environments in the presence and absence of iron carbonate films.* Wear, 2018. **404-405**: p. 143-152.

33.   Phares, D.J., G.T. Smedley, and R.C. Flagan, *The wall shear stress produced by the normal impingement of a jet on a flat surface.* Journal of Fluid Mechanics, 2000. **418**: p. 351-375.

34.   Durst, F., D. Miloievic, and B. Schönung, *Eulerian and Lagrangian predictions of particulate two-phase flows: a numerical study.* Applied Mathematical Modelling, 1984. **8**(2): p. 101-115.

35.   Clift, R., J.R. Grace, and M.E. Weber, *Bubbles, drops, and particles*. 1978, London: Academic Press.

36.   Mansouri, A., H. Arabnejad, S. Karimi, S.A. Shirazi, and B.S. McLaury, *Improved CFD modeling and validation of erosion damage due to fine sand particles.* Wear, 2015. **338–339**: p. 339-350.

37.   Wang, J. and S.A. Shirazi, *A CFD Based Correlation for Erosion Factor for Long-Radius Elbows and Bends.* Journal of Energy Resources Technology, 2003. **125**(1): p. 26-34.

38.   Douglas, J.F., J.M. Gasiorek, J.A. Swaffield, and L.B. Jack, *Fluid Mechanics*. 5th ed. 2005, Harlow: Pearson/Prentice Hall.

39.   Humphrey, J.A.C., *Fundamentals of fluid motion in erosion by solid particle impact.* International Journal of Heat and Fluid Flow, 1990. **11**(3): p. 170-195.

40.   Naim, M. and S. Bahadur, *Work hardening in erosion due to single-particle impacts.* Wear, 1984. **98**: p. 15-26.

41.   Rajahram, S.S., T.J. Harvey, J.C. Walker, S.C. Wang, and R.J.K. Wood, *Investigation of erosion–corrosion mechanisms of UNS S31603 using FIB and TEM.* Tribology International, 2012. **46**(1): p. 161-173.

42.   Hutchings, I.M. and P. Shipway, *Tribology: Friction and Wear of Engineering Materials*. 2nd ed. 2017, London: Butterworth-Heinemann.

Erosion-corrosion interactions of X65 carbon steel in aqueous CO₂ environments

Supplementary Material

Joshua Owen[a], Callum Ramsey[b], Richard Barker[a], Anne Neville[a]

a Institute of Functional Surfaces, School of Mechanical Engineering, University of Leeds, Leeds, LS2 9JT, United Kingdom
b Shell U.K. Limited, 1 Altens Farm Road, Nigg, Aberdeen, AB12 3FY, United Kingdom

1. Fluid Flow CFD Model

A common methodology for CFD models of particle trajectories was used for the development of the model in this paper whereby the flow model was developed and solved before particles trajectories were predicted [1, 2]. The fluid flow out of the 2D axisymmetric nozzle was predicted using the k-ω turbulence model, with this turbulence model being preferred to the k-ε model due to the k-ε model's limitations in predicting flow in axisymmetric jets [3]. Due to the relatively large size of the sand particles used in particle trajectory predictions compared to the thickness of boundary layers, a turbulence model using wall functions was acceptable to use [4]. A mesh sensitivity analysis of this model was completed and showed that a mesh consisting of 81,911 first order triangular bulk domain and rectangular boundary elements gave sufficient accuracy, as shown in Figure 1 where the shear stress was predicted across the sample surface and compared with an analytical solution of shear stress, Equation (**1**) [5, 6]. Equation (**1**) is only applicable in certain conditions, therefore the nozzle diameter was adjusted to give a ratio of nozzle height to nozzle diameter (H/d_N) of 2 and a region on the surface was analysed at a ratio of greater than 2.5 for the distance from the centre of the nozzle to the nozzle diameter (r/d_N). No appropriate equation was available to predict the shear stress for the nozzle geometry used in erosion-corrosion testing in this work. Results were not sensitive to the element order. The number of elements shown in Figure 1 was different to the number of elements used for the predictions using a 4 mm diameter nozzle due to the slight difference in geometry. However, the same mesh parameters were used for the smaller diameter nozzle used for predictions at 20 m/s with a 4 mm diameter nozzle.

$$\frac{\tau_w Re_J^{1/2} \left(\frac{H}{d_N}\right)^2}{\rho_f U^2} = 0.34 Re_J^{1/5} \left(\frac{r}{H}\right)^{-2.3} \tag{1}$$

where τ_w is the wall shear stress, ρ_f is the fluid density, U is the flow velocity, and Re_J is the Reynolds jet number defined in Equation (**2**).

$$Re_J = \frac{\rho U d_N}{\mu} \tag{2}$$
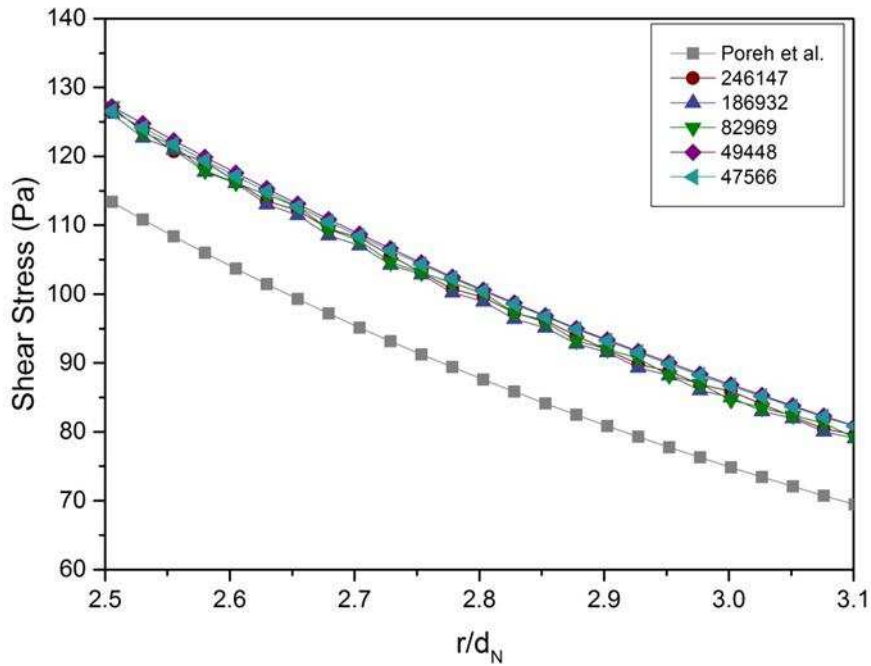
where μ is the dynamic viscosity.

Figure 1: CFD prediction of shear stress across the surface of a SIJ sample for a H/d$_N$ ratio of 2 at a flow velocity of 8 m/s at 60°C compared with an analytical solution for shear stress in an axisymmetric impinging jet [6]

2. Particle Trajectory Predictions

The individual forces used in the equation of motion for particle trajectory predictions are defined. The drag force acting on the particle is defined as:

$$F_d = C_D \frac{\pi d_p^2}{8} \rho_f (U - v_p)|U - v_p| \tag{3}$$

where d_p is the particle diameter, v_p is the particle velocity and C_D is the drag coefficient defined as:

$$C_D = \frac{24}{Re_p}\left(1 + 0.15 Re_p^{0.687}\right) \tag{4}$$

The particle Reynolds number, Re_p, is defined as:

$$Re_p = \frac{\rho_f}{\mu}|U - v_p|d_p \qquad (5)$$

The pressure gradient force is defined as:

$$F_p = \frac{1}{4}\pi d_p^3 \nabla p \qquad (6)$$

where ∇p is the divergence of pressure. The buoyancy force is defined as:

$$F_b = \frac{1}{6}\pi d_p^3 (\rho_p - \rho_f)g \qquad (7)$$

where ρ_p is the density of the particle and g is acceleration due to gravity. The added mass force is defined as:

$$F_a = -\frac{1}{12}\pi d_p^3 \rho_p \frac{dv_p}{dt} \qquad (8)$$

The following assumptions were made to simplify the model, similar to the assumptions made in other particle trajectory CFD models [1, 2]:

- Particles were assumed to be spherical in shape with a diameter of 250 μm. The sand particles used experimentally had a range of sizes from approximately 100 μm to 500 μm, with approximately 70% of the particles in the size range from 180 μm - 320 μm. Therefore, some variation in impact angles and impact velocities on the surface of the sample was expected. Lynn et al. [7] showed how changes in particle size had a significant effect on the erosion rate, but had less significance on the impact velocity. The model developed in this work was only used to predict impact velocities and angles, and not to calculate erosion rates, therefore this assumption was not expected to be significant for the range of particle sizes used experimentally. Particles were shown to be irregular in shape which could influence the drag force. However, modelling the individual shapes would not be feasible due to a lack of available drag force models for unique shapes of sand particles and would require intensive computational resources

- All surfaces were assumed to be smooth. Surface texture would have significantly increased the complexity of the model and validation of the model would have proved difficult. The surface texture was also expected to change during testing, as erosion had been shown to increase surface roughness of metal specimens [8]

- The surface of the sample was assumed to remain flat throughout a test. Test duration was short enough to ensure that wear scars on the surface of the sample did not get so large to significantly change impact angles and velocities. Wear depth was shown to be smaller than the diameter of sand particles, therefore was not expected to significantly change particle trajectories. The surface would also be constantly changing during test, making modelling of the surface complicated and difficult to validate

- Particles were assumed to be evenly distributed over the entire width of the nozzle inlet diameter, when entering the nozzle. Due to the random nature of the sand particle trajectories as they enter the nozzle and inability to validate their position, it is unknown exactly how the particles enter the nozzle. The simplest assumption that particles were evenly distributed over the inlet was used as no evidence exists to suggest the particles enter the nozzle in any other manner.

- Particles did not influence the fluid flow due to the low volume percentage of particles in the flow. This assumption is valid for low sand concentrations [9]

- Particle-particle interactions were also considered negligible, an acceptable assumption due to the low sand concentration [10]

- Particles were assumed to have a starting velocity equivalent to the flow velocity at the inlet

- During each cycle of particle impacts, particles were assumed to only impinge on the surface once before being transported by the fluid from the sample and into the fluid reservoir domain without impacting the surface again

- The effects of the squeeze film reducing impact velocity and impact frequency suggested by Clark [11] were assumed to be insignificant in these conditions due to the high flow velocities and low viscosity of the water at a temperature 60°C. Ukpai et al. [12] showed using acoustic emission monitoring in the SIJ with the exact same geometry that the number of impacts on the surface of a carbon steel sample was similar to the predicted number of impacts, suggesting the majority of sand particles impacted once on the surface as expected.

References

1.   Chen, X., B.S. McLaury, and S.A. Shirazi, *Application and experimental validation of a computational fluid dynamics (CFD)-based erosion prediction model in elbows and plugged tees.* Computers & Fluids, 2004. **33**(10): p. 1251-1272.

2.   Gnanavelu, A., N. Kapur, A. Neville, and J.F. Flores, *An integrated methodology for predicting material wear rates due to erosion.* Wear, 2009. **267**(11): p. 1935-1944.

3.   Versteeg, H.K. and W. Malalasekera, *An introduction to computational fluid dynamics: the finite volume method*. 2007, Harlow: Pearson Education.

4.   Mansouri, A., H. Arabnejad, S. Karimi, S.A. Shirazi, and B.S. McLaury, *Improved CFD modeling and validation of erosion damage due to fine sand particles.* Wear, 2015. **338–339**: p. 339-350.

5.   Phares, D.J., G.T. Smedley, and R.C. Flagan, *The wall shear stress produced by the normal impingement of a jet on a flat surface.* Journal of Fluid Mechanics, 2000. **418**: p. 351-375.

6.   Poreh, M., Y. Tsuei, and J.E. Cermak, *Investigation of a turbulent radial wall jet.* Journal of Applied Mechanics, 1967. **34**(2): p. 457-463.

7.   Lynn, R.S., K.K. Wong, and H.M. Clark, *On the particle size effect in slurry erosion.* Wear, 1991. **149**(1-2): p. 55-71.

8.   Finnie, I., *Erosion of surfaces by solid particles.* Wear, 1960. **3**(2): p. 87-103.

9.   Brown, G., *Erosion prediction in slurry pipeline tee-junctions.* Applied Mathematical Modelling, 2002. **26**(2): p. 155-170.

10.   Humphrey, J.A.C., *Fundamentals of fluid motion in erosion by solid particle impact.* International Journal of Heat and Fluid Flow, 1990. **11**(3): p. 170-195.

11.   Clark, H.M., *The influence of the squeeze film in slurry erosion.* Wear, 2004. **256**(9): p. 918-926.

12.   Ukpai, J.I., R. Barker, X. Hu, and A. Neville, *Determination of particle impacts and impact energy in the erosion of X65 carbon steel using acoustic emission technique.* Tribology International, 2013. **65**(0): p. 161-170.